Combustion and Flame 212 (2020) 93–106

Contents lists available at ScienceDirect

Combustion and Flame

journal homepage: www.elsevier.com/locate/combustflame

Transient ellipsoidal combustion model for a porous burner in microgravity

Akshit Markan, Howard R. Baum, Peter B. Sunderland, James G. Quintiere*, John L. de Ris

Department of Fire Protection Engineering, University of Maryland, College Park, 3104 J.M. Patterson Building, College Park, MD 20742, USA

ARTICLE INFO

Article history:
Received 3 January 2019
Revised 24 September 2019
Accepted 24 September 2019

Keywords:
Diffusion flames
Laminar flames
Flame shapes
Fire safety

ABSTRACT

The current study develops a transient combustion model formulated in oblate ellipsoidal coordinates to analyze the behavior of non-buoyant burner-generated diffusion flames. The combustion model is axially symmetric and considers a porous gas-fueled burner called the Burning Rate Emulator (BRE), which is idealized as an ellipsoidal disk. An approximate analytical transient solution for the flame shape and heat transfer to the surface of the burner is generated as a product of the exact steady-state result and the asymptotic transient result that becomes exact far from the burner. Microgravity BRE experiments conducted at NASA Glenn's 5.18-s Zero Gravity Research Facility indicated the evolution of an approximately ellipsoidal flame moving away from the burner with steady state not achieved during the 5-second test period. The microgravity experimental results are shown to be in good agreement with the mathematical model, which can help predict the flame behavior beyond the duration of the test.

Published by Elsevier Inc. on behalf of The Combustion Institute.

1. Introduction

A porous circular burner has been recently developed to emulate the combustion of condensed phase fuels in normal gravity [1] and microgravity conditions [2–4]. Known as the Burning Rate Emulator (BRE), it uses a gaseous fuel mixture as the simulant fuel with matching characteristic properties such as heat of gasification, heat of combustion, surface vaporization temperature, and smoke point. Experiments using the burner were conducted at NASA Glenn's 5.18-s Zero Gravity Research Facility in order to establish immediate sustained burning and provide a material flammability test aboard spacecraft. The burner sizes and parameters for the microgravity tests were chosen to represent small laminar pool fires. The aim of the current study is to develop a simple yet robust mathematical model and demonstrate its utility for such a diffusion flame in microgravity conditions.

The fuel flow through the BRE burner is set to generate laminar diffusion flames that provide an easy way to assess fire behavior in microgravity. Low momentum jet diffusion flames are probably the closest in configuration to the BRE generated diffusion flames. The jet flame microgravity experiments with low Reynolds number have been analyzed theoretically and numerically using an axisymmetric cylindrical model [5–18]. The analyses primarily relied on the Burke–Schumann model [19], Roper model [20,21] or the Spalding model [22]. These basic models, while effective, provided only steady-state conditions.

The BRE flames had an ellipsoidal shape during the 5-s microgravity experiment and their aspect ratios decreased with time [2,3]. Steady flames were not attained during the tests [3]. Longer duration experiments have been planned on the International Space Station (ISS) to find out if further flame growth would lead to a steady flame or extinction [23]. The motivation of the current work is to mathematically examine the transient aspects of the BRE microgravity flames, focusing on flame growth and not flame extinction. That approach is based on a solution evolved from that of a spherical flame.

As a spherical diffusion flame is considered as an important first step in the formation of the BRE transient model, it is important to review that body of work. Spherical steady flames have been theoretically elucidated by Mills and Matalon [24,25]. The transient aspects of spherical flames in microgravity have been studied extensively using NASA's 2.2 S Drop Tower with numerical analyses [26–33]. Atreya and coworkers [26–30] developed a finite-difference based theoretical model for an unsteady spherical diffusion flame to understand radiation-induced flame extinction characteristics in a quiescent microgravity environment. Tse et al. [31] and Santa et al. [32,33] also studied the transient structure of burner-generated spherical diffusion flames using a computational model based on a modification of the Sandia PREMIX code [34].

Other flame geometries have been studied by computational modeling. For example, Bhowal and Mandal [35] carried out an in-depth two-dimensional computational analysis of a laminar

* Corresponding author.
E-mail address: jimq@umd.edu (J.G. Quintiere).

https://doi.org/10.1016/j.combustflame.2019.09.030
0010-2180/Published by Elsevier Inc. on behalf of The Combustion Institute.

Nomenclature

a	semi-major axis
b	semi-minor axis
c	quantity to relate cylindrical and ellipsoidal coordinates
c_p	specific heat
D	burner diameter
$\mathcal{D}$	diffusivity
h	grid spacing
Δh_c	heat of combustion per mass of fuel
k	thermal conductivity
Le	Lewis number
$\dot{m}''$	fuel mass flux, or burning rate
$\dot{M}$	surface mass flow rate
p	pressure
Pe	Peclet number
$\dot{q}''$	heat flux
r	radius
R	burner radius
R^*	offset radius
S	stoichiometric ratio
t	time
T	temperature
u	velocity
x	x coordinate
y	dimensionless radius
Y	mass fraction
y_f	flame height
Z	mixture fraction

Greek

ϵ	aspect ratio of the ellipsoidal object
η	ellipsoidal coordinate, or similarity variable
θ	dimensionless temperature
μ	viscosity
ξ	ellipsoidal coordinate
ρ	density
τ	dimensionless time
ϕ	velocity potential
ω	vorticity

Subscripts

F	fuel
Fb	fuel at burner surface
fl	flame
o	burner surface
O	oxygen
P	products
Pb	products at burner surface
s	surface
∞	ambient

non-premixed jet flame in reduced gravity conditions. A similar 2D numerical model was developed by Smooke et al. [36,37] for an axisymmetric laminar diffusion flame over a cylindrical coflow burner in earth gravity.

The current work aims to develop an approximate analytical solution for the transient BRE microgravity flame instead of a numerical analysis to gain a better understanding of the fluid dynamics-thermochemistry interaction in a non-spherical geometry and its effect on the flame structure. The analytical model also clearly reveals generalities in results and permits its accurate assessment, a task that should also accompany a numerical solution. The BRE diffusion combustion problem is simplified by neglecting gas radiation and presence of soot as well as assuming an infinitely thin zone of the chemical reaction. Fursenko et al. [38] made similar assumptions to analytically model a steady spherical diffusion microflame.

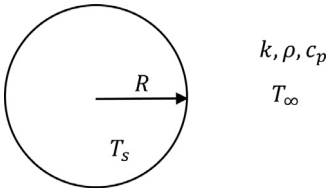

Fig. 1. Schematic of heated sphere without flow.

The analytical model for the combustion problem is developed in stages. This is done to demonstrate the analytical approach and to establish a firm confidence level for the combustion solution. First, the transient spherical conduction problem of a heated sphere in a cold gas is presented since it depicts the mathematical similarity to the combustion problem. This problem is also used to introduce the crucial approximation needed to develop analytical solutions. The non-spherical geometry of the flame is then considered by strategically introducing oblate ellipsoidal coordinates. These coordinates still maintain the one-dimensional simplicity to the problem but help generate ellipsoidal flames as observed experimentally. The solution to the conduction problem can be broken down into components that can be generalized to the combustion problem using a model based on the burning of small particles formulated in ellipsoidal coordinates [39,40]. Thus, the ellipsoidal combustion model delivers an analytical description of the different combustion features. The difference between the approximate analytical results and numerical results are calculated for the conduction problems with and without blowing to demonstrate the accuracy of the modeling approach. The final combustion problem is then solved to obtain the results that are compared to the BRE 5-s microgravity experiments. If the reader is not interested in the justification of the modeling approach, then one can proceed directly to Section 5.

2. Spherical conduction problem without flow

To begin, a heated sphere at temperature T_s immersed in a cool environment is considered with ambient temperature T_∞. The sphere has a radius R and the environment has a specific heat c_p, density ρ and thermal conductivity k. There is no flow through the sphere and it transfers heat to the surroundings only through conduction. The schematic of the heated sphere is as shown in Fig. 1.

The aim is to find a transient analytical solution for the temperature T as a function of distance r from the center of the sphere. A dimensionless temperature θ is defined for solving this problem as follows:

$$\theta = \frac{T - T_\infty}{T_s - T_\infty} \tag{1}$$

The governing equation in this case is the heat conduction equation [41] which could be written as,

$$\rho c_p \frac{\partial \theta}{\partial t} = \frac{1}{r^2}\frac{\partial}{\partial r}\left(kr^2 \frac{\partial \theta}{\partial r}\right) \tag{2}$$

The radial distance r and time t are nondimensionalized to provide the dimensionless distance y and dimensionless time τ.

$$y = \frac{r}{R}, \quad \tau = \frac{kt}{\rho c_p R^2} \tag{3}$$

This simplifies the heat conduction equation in terms of all non-dimensional variables.

$$\frac{\partial\theta}{\partial\tau} = \frac{1}{y^2}\frac{\partial}{\partial y}\left(y^2\frac{\partial\theta}{\partial y}\right) \tag{4}$$

The initial and boundary conditions need to be defined for this problem. The initial temperature, i.e., the temperature at $t = 0$ is the ambient temperature T_∞ everywhere around the sphere. The boundary conditions are defined at the surface of the sphere and at a distance far from the burner ($y \to \infty$). The temperature at the surface of the sphere is the preset temperature T_s while the temperature far from the sphere is the ambient temperature T_∞. These conditions can be written in non-dimensional form as shown below.

$$\theta(\tau = 0, y > 1) = 0 \tag{5a}$$

$$\theta(\tau, y = 1) = 1 \tag{5b}$$

$$\lim_{y\to\infty}\theta(\tau, y) = 0 \tag{5c}$$

The heat conduction equation has a similarity variable solution elucidated in literature [42], and it can be expressed as,

$$\theta = \frac{1}{y}\text{erfc}\left(\frac{y-1}{2\sqrt{\tau}}\right). \tag{6}$$

This result suggests that the solution for temperature is the product of its steady state result and the transient component. It will be shown that this is an expected solution form for the problems considered here.

Also, the surface heat flux is given as,

$$\dot{q}_s'' = \frac{k(T_s - T_\infty)}{R} + \frac{k(T_s - T_\infty)}{R\sqrt{\pi\tau}}. \tag{7}$$

Here, the surface heat flux, a key parameter in the combustion solution, is represented as the sum of the steady solution and its transient component.

3. Heated sphere problem with blowing

The form of the solution obtained above provides the motivation for the remainder of the analysis. Note that the term $1/y$ in Eq. (6) is in fact the exact steady state solution to the problem. The complete solution is the product of the steady state solution that is dominant near the surface of the sphere at $r = R$, and the transient solution dominant far from the sphere.

To illustrate this solution behavior let us examine a conduction problem approaching the nature of the more complex combustion problem. Consider a porous sphere at temperature T_s with fluid flowing out of the surface at a constant rate with ambient temperature T_∞. The sphere has a radius R and the environment has a specific heat c_p, density ρ and thermal conductivity k that are here considered to be constant. The schematic of the sphere is as shown in Fig. 2.

The fluid carries heat by conduction and convection due to the motion of the fluid. The spherical symmetry makes the model a one-dimensional problem. The desired quantity is the transient temperature T as a function of the radial distance r and the fluid flow. A dimensionless temperature θ is again defined for solving this problem as follows:

$$\theta = \frac{T - T_\infty}{T_s - T_\infty} \tag{8}$$

The governing equations for this case are the continuity equation and the energy equation. The continuity equation is given below where $\dot{m}_o''$ is the mass flux at the surface which is a constant.

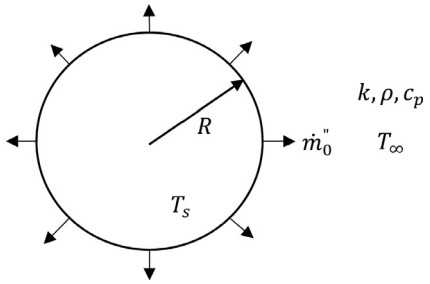

Fig. 2. Schematic of the spherical combustion model.

$$r^2\rho u = r^2\dot{m}'' = R^2\dot{m}_o'' = \text{constant} \tag{9}$$

The energy equation for the fluid with conduction and convection heat transfer is given as,

$$r^2\rho c_p\frac{\partial\theta}{\partial t} + r^2\rho c_p u\frac{\partial\theta}{\partial r} = \frac{\partial}{\partial r}\left(kr^2\frac{\partial\theta}{\partial r}\right) \tag{10}$$

The radial distance r, time t and surface mass flux $\dot{m}_o''$ are nondimensionalized as follows:

$$y = \frac{r}{R},\ \tau = \frac{kt}{\rho c_p R^2},\ \text{Pe} = \frac{\dot{m}_o'' R c_p}{k} \tag{11}$$

This simplifies the energy equation in terms of all non-dimensional variables.

$$\frac{\partial\theta}{\partial\tau} = \frac{\partial^2\theta}{\partial y^2} + \frac{(2y - \text{Pe})}{y^2}\frac{\partial\theta}{\partial y} \tag{12}$$

Note that Pe is the Peclet number for this problem. The initial and boundary conditions are similar to the previous model and can be written in non-dimensional form as shown below.

$$\theta(\tau = 0, y > 1) = 0 \tag{13a}$$

$$\theta(\tau, y = 1) = 1 \tag{13b}$$

$$\lim_{y\to\infty}\theta(\tau, y) = 0 \tag{13c}$$

3.1. Composite solution

This section now builds on the solution form of the non-blowing problem as given in Eq. (6). The solution is considered to be the product of the exact steady state solution and the asymptotic transient solution in the far field. The accuracy of this approximation will be shown based on a numerical solution to the full equations of Eqs. (12) and (13) together with an error analysis of the approximate solution.

The steady state solution for Eq. (12) is obtained and it is given as,

$$\theta = \frac{\exp(-\text{Pe}/y) - 1}{\exp(-\text{Pe}) - 1}. \tag{14}$$

The effect of fluid flow becomes negligible far from the sphere and hence, in Eq. (12) the term with $1/y^2$ can be neglected. This asymptotic equation is the pure conduction problem of Eq. (4). Its solution is repeated here as,

$$\theta = \frac{1}{y}\text{erfc}\left(\frac{y-1}{2\sqrt{\tau}}\right). \tag{15}$$

Now the assumption for the approximate solution as made up of the steady result with the product of the asymptotic transient result for y large is invoked. Therefore, the transient composite solution for Eq. (12) is achieved by replacing $(1/y)$ in Eq. (15) with

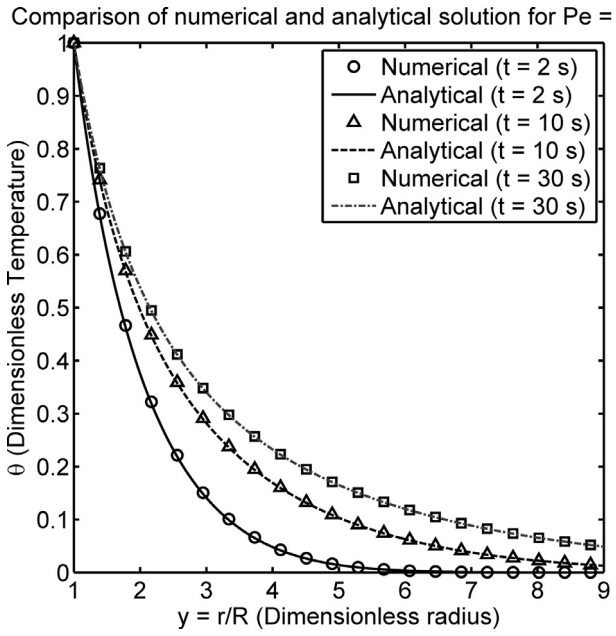

Fig. 3. Dimensionless temperature vs radius for Pe = 0.79 (spherical conduction model).

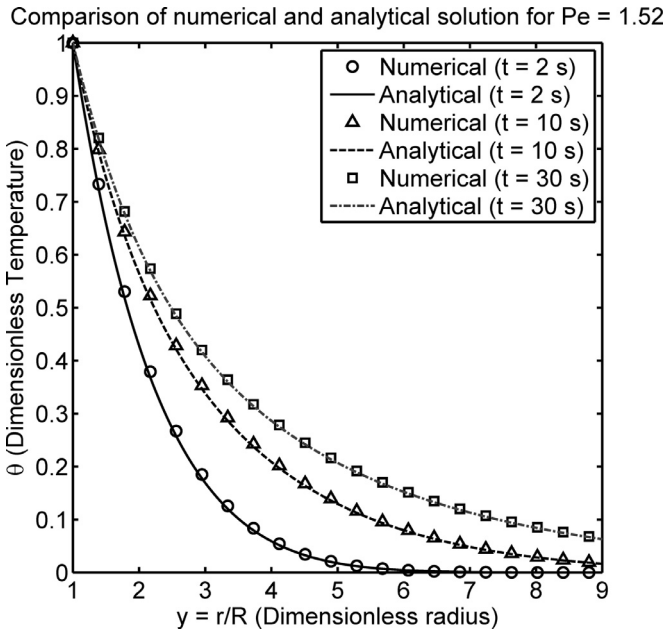

Fig. 4. Dimensionless temperature vs radius for Pe = 1.52 (spherical conduction model).

the steady state solution given in Eq. (14). It is important to note that the steady state solution given by Eq. (14) is proportional to $1/y$ for large y so that Eq. (15) is satisfied. Thus, the composite solution is the product of the steady state solution and its transient solution far from the sphere. Explicitly the approximate solution is given as

$$\theta = \left(\frac{\exp(-\mathrm{Pe}/y) - 1}{\exp(-\mathrm{Pe}) - 1}\right)\mathrm{erfc}\left(\frac{y-1}{2\sqrt{\tau}}\right). \tag{16}$$

3.2. Numerical solution

Eq. (12) is solved numerically to determine the accuracy of Eq. (16). The equation is a second order partial differential equation that is semi-discretized. This results in a system of ordinary differential equations that can be readily solved using a numerical method for ODEs based on the 2nd order central difference formula. The semi-discretized form of Eq. (12) looks like,

$$\left(\frac{d\theta}{d\tau}\right)_i = \frac{\theta_{i+1} - 2\theta_i + \theta_{i-1}}{h^2} + \left(\frac{2y_i - \mathrm{Pe}}{y_i^2}\right)\left(\frac{\theta_{i+1} - \theta_{i-1}}{2h}\right) \tag{17}$$

3.3. Direct comparison of the approximate and numerical results

To check the accuracy of the composite solution, it is compared with the numerical solution for two particular cases. The cases correspond to two mass fluxes that range the data of the combustion problem used during the 5-s microgravity experiments [2,3]. A sphere of diameter 25 mm has a fluid flowing through it. The two cases are a surface mass flux of $\dot{m}_0'' = 3.582$ g/m^2–s corresponding to a Peclet number of 0.79, and case for a surface mass flux of $\dot{m}_0'' = 6.887$ g/m^2–s corresponding to a Peclet number of 1.52. The environmental properties are taken for Nitrogen at 1000 K. To compare the results, the numerical analysis is run for up to 30 s and the dimensionless temperature is recorded as a function of dimensionless radius at every time step. Figures 3 and 4 compare the variation of numerical and the approximate analytical dimensionless temperature with dimensionless radius for both Peclet numbers at three different times: 2 s, 10 s and 30 s. It can be seen that the analytical and numerical solutions coincide in all regions, i.e., near the sphere, in far field and in between. The approximate solution is within 0.5% of the numerical results.

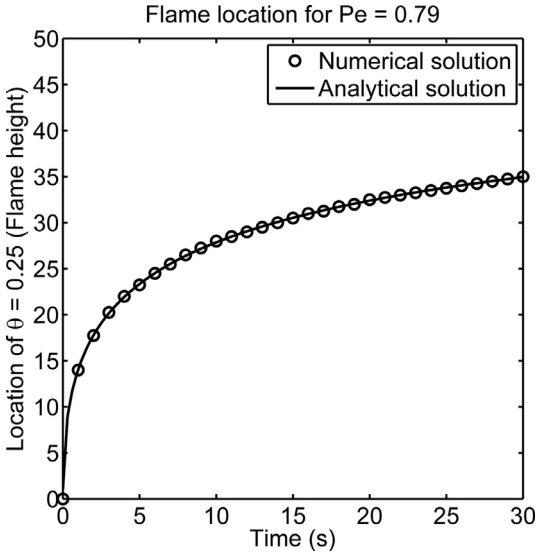

Fig. 5. Transient flame standoff (in mm) for Pe = 0.79 (spherical conduction model).

Also let us use the conduction problem to represent the combustion problem with the flame sheet located where the dimensionless temperature is 0.25. The position of this represents the location of the flame at $(r - R)$ and could be determined as a function of time. We do this in anticipation of using the composite approximate solution for the combustion, and wish to check the accuracy in determining the 'flame location'. Figures 5 and 6 compare the numerical and analytical flame position (0.25) with time for both Peclet numbers. Again, the numerical and analytical solutions in this case are within 0.5% of each other and the error reduces with time. This depicts the reliability and accuracy of the analytical model for both the dependent variable and its locus position.

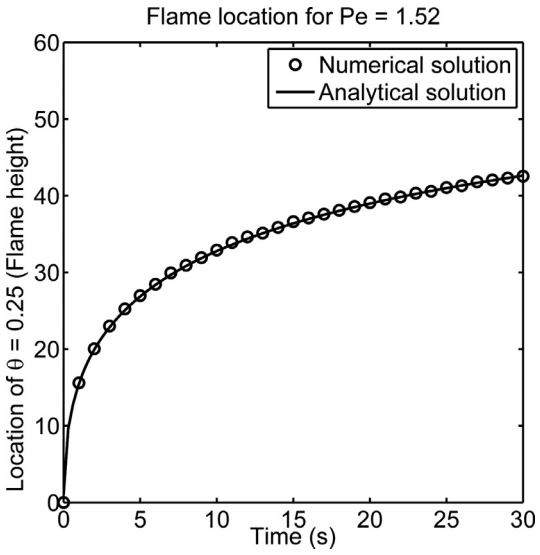

Fig. 6. Transient flame standoff (in mm) for Pe = 1.52 (spherical conduction model).

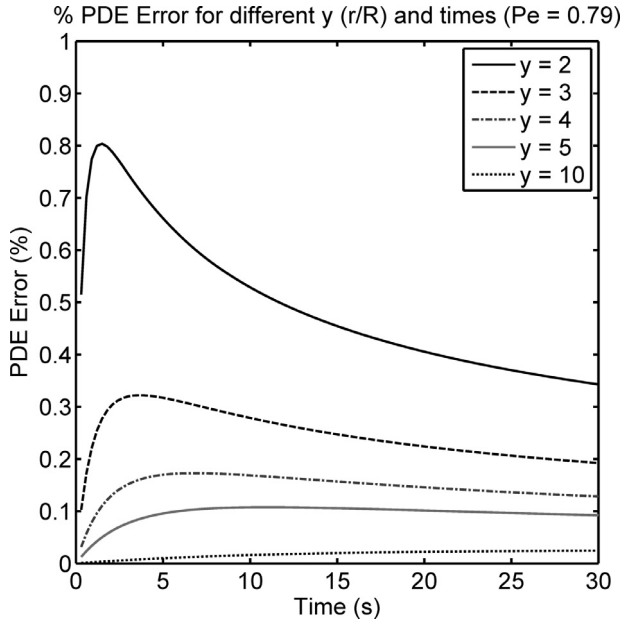

Fig. 7. PDE Error% for the composite solution to the spherical conduction problem with flow (Pe = 0.79).

3.4. Accuracy by substitution method

Another method to verify the accuracy of the composite solution is to substitute Eq. (16) in the PDE given by Eq. (12). The discrepancy in the solution, i.e. the amount by which the equation is not satisfied, is compared with the magnitude of the largest term in the equation. The ratio of the two is a measure of the error. The error in the PDE is determined as a function of time for different values of y (r/R). It is considered for a sphere of diameter 25 mm having a surface mass flux of $\dot{m}_o'' = 3.582$ g/m^2 – s, which corresponds to a Peclet number of 0.79. The PDE substitution error is shown in Fig. 7. It can be seen that the error is less than 1% for all radial positions and at all times. This error estimate is consistent with the accuracy of the numerical results shown here.

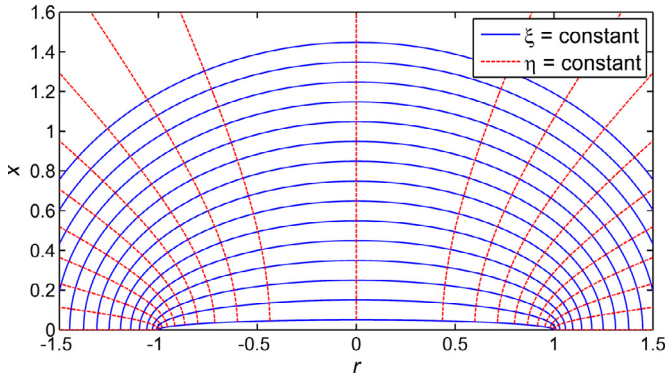

Fig. 8. Oblate Ellipsoidal Coordinate System for $\epsilon = 0.05$.

4. Heated ellipsoid problem with blowing

In anticipation to the combustion problem, the conduction problem for an ellipsoidal object with blowing is considered. Oblate ellipsoids of revolution are considered here that range in shape from a sphere to a thin disk. The spherical shape has been addressed in Section 3, and the combustion problem will be represented as a thin disc. Fluid is emitted at the heated surface of a porous oblate ellipsoid particle with a constant mass flow rate $\dot{M}$. The starting point is to introduce the oblate ellipsoidal coordinate system.

4.1. Oblate ellipsoidal coordinates

The cylindrical coordinate system in (x, r) is represented for an ellipsoidal object as shown in Fig. 8. The oblate ellipsoid is symmetric about the x axis and has a semi-major axis a and a semi-minor axis b. The semi-major axis can be written as $a = R$.

The problem can be converted from cylindrical coordinates to oblate ellipsoidal dimensionless coordinates given by (ξ, η) as illustrated in Fig. 8. This will simplify the problem for an ellipsoidal object with blowing at its surface. The system aligns with the cylindrical coordinate system such that the surface of the ellipsoid object is defined by $\xi = \xi_o$. The two coordinate systems are related by a length c as shown here:

$$r^2 = c^2\left(1+\xi^2\right)\left(1-\eta^2\right) \tag{18a}$$

$$x = c\xi\eta \tag{18b}$$

The quantity c can be related to the semi-major and semi-minor axis as follows:

$$a = c\sqrt{1+{\xi_o}^2},\ \ b = c\xi_o \tag{19}$$

The oblate ellipsoidal surface in cylindrical coordinates can be written as,

$$\frac{r^2}{c^2\left(1+{\xi_o}^2\right)} + \frac{x^2}{\left(c\xi_o\right)^2} = 1 \tag{20}$$

An aspect ratio ϵ is introduced as the ratio of the semi-minor axis to the semi-major axis. Then the quantities c and ξ_o can be written in terms of the aspect ratio as follows:

$$\xi_o = \frac{\epsilon}{\sqrt{1-\epsilon^2}},\ \ c = R\sqrt{1-\epsilon^2} \tag{21}$$

Figure 8 shows the oblate ellipsoidal coordinate system for $\epsilon = 0.05$ or $\xi_o = 0.0501$. The oblate ellipsoidal coordinates can be written in terms of cylindrical coordinates as follows:

$$\xi = \frac{1}{\sqrt{2}c}\left[x^2 + r^2 - c^2 + \sqrt{\left(x^2 + r^2 - c^2\right)^2 + (2xc)^2}\right]^{\frac{1}{2}}, \quad \eta = \frac{x}{c\xi} \tag{22}$$

4.2. Governing equations

The ellipsoid surface is at a constant temperature T_s while the ambient temperature is fixed at T_∞. Here we will assume that the density ρ and (thermal) diffusivity $\mathcal{D} \equiv k/\rho c_p$ are constant. That assumption will be relaxed in the combustion problem later. The objective is to obtain the transient temperature domain for the fluid surrounding the ellipsoid of revolution by our approximate method.

This model follows the previous spherical conduction model where the dimensionless temperature is given as $\theta = (T - T_\infty)/(T_s - T_\infty)$ and the velocity vector as $\vec{u}$. Under constant property assumptions, the governing equations from the conservation of mass and energy become:

$$\nabla \cdot (\vec{u}) = 0 \tag{23a}$$

$$\frac{\partial \theta}{\partial t} + \nabla \cdot (\vec{u}\theta) - \mathcal{D}\nabla \cdot (\nabla\theta) = 0 \tag{23b}$$

The conservation of mass equation can be solved assuming that the flow field is irrotational. This follows from the momentum equation for a constant viscosity [41]:

$$\rho\left[\frac{\partial \vec{u}}{\partial t} + \vec{\omega} \times \vec{u} + \nabla(\vec{u})^2/2\right] + \nabla(p - p_\infty)$$
$$= -\mu(\nabla \times \vec{\omega}) + \frac{4}{3}\mu\nabla(\nabla \cdot \vec{u}) \tag{24}$$

Here, $\vec{\omega}$ is the vorticity and p is the pressure related to the flow field. If the vorticity vanishes then the velocity potential ϕ can be introduced such that:

$$\vec{u} = \nabla\phi, \ \vec{\omega} = 0 \tag{25}$$

This momentum equation can be integrated such that $p - p_\infty$ and $\vec{u}$ vanish for r large. The result is the generalized Bernoulli equation.

$$\rho\left(\frac{\partial \phi}{\partial t} + (\vec{u}.\vec{u})/2\right) + (p - p_\infty) - \frac{4}{3}\mu(\nabla \cdot \vec{u}) = 0 \tag{26}$$

The velocity satisfies the no-slip boundary condition so long as the velocity potential ϕ is a function of ξ everywhere. Substitution of Eq. (25) into the mass and energy conservation equations yields:

$$\nabla^2\phi = 0 \tag{27a}$$

$$\frac{\partial \theta}{\partial t} + \nabla \cdot (\theta\nabla\phi) - \mathcal{D}\nabla^2\theta = 0 \tag{27b}$$

In order to explicitly express the above equations in oblate ellipsoidal coordinates, it is necessary to express the divergence of a vector $\vec{f}(\xi, \eta) = (f_\xi, f_\eta)$ and the gradient of a scalar $g(\xi, \eta)$. Mathematically,

$$\nabla \cdot \vec{f} = \frac{1}{c\left(\xi^2 + \eta^2\right)}\left\{\frac{\partial}{\partial \xi}\left[\sqrt{\left(\xi^2 + \eta^2\right)\left(\xi^2 + 1\right)}f_\xi\right] + \frac{\partial}{\partial \eta}\left[\sqrt{\left(\xi^2 + \eta^2\right)\left(1 - \eta^2\right)}f_\eta\right]\right\} \tag{28a}$$

$$\nabla g = \frac{1}{c}\sqrt{\frac{\left(\xi^2 + 1\right)}{\left(\xi^2 + \eta^2\right)}}\frac{\partial g}{\partial \xi}\vec{i}_\xi + \frac{1}{c}\sqrt{\frac{\left(1 - \eta^2\right)}{\left(\xi^2 + \eta^2\right)}}\frac{\partial g}{\partial \eta}\vec{i}_\eta \tag{28b}$$

The no-slip condition at the surface requires that the velocity potential have no component parallel to any surface of constant ξ and the velocity vectors are aligned in the direction of increasing ξ. Then from Eq. (28b), the velocity vector $\vec{u}$ and its divergence can be expressed in ellipsoidal coordinates as:

$$\vec{u} = \nabla\phi = \frac{1}{c}\sqrt{\frac{\left(\xi^2 + 1\right)}{\left(\xi^2 + \eta^2\right)}}\frac{d\phi}{d\xi}\vec{i}_\xi \tag{29a}$$

$$\nabla \cdot \vec{u} = \nabla^2\phi = \frac{1}{c^2\left(\xi^2 + \eta^2\right)}\frac{d}{d\xi}\left[\left(\xi^2 + 1\right)\frac{d\phi}{d\xi}\right] \tag{29b}$$

Substituting Eq. (29b) in Eq. (27a), the mass conservation equation takes the form:

$$\frac{d}{d\xi}\left[\left(\xi^2 + 1\right)\frac{d\phi}{d\xi}\right] = 0 \tag{30}$$

This equation can be integrated at the surface of the ellipsoid where the mass flow rate is $\dot{M}$.

$$\left(\xi^2 + 1\right)\frac{d\phi}{d\xi} = \frac{\dot{M}}{4\pi c\rho} \tag{31}$$

Note that here the mass flow rate is over the entire ellipsoidal object. The solution of this equation for ϕ can be continued, but instead we focus on the solution of the energy equation for θ.

To express the energy conservation equation for the fluid in ellipsoidal coordinates, derivatives of temperature θ with respect to η are ignored as it is anticipated that the solution to be constructed is a function only of ξ and time. The various components of the energy conservation equation can be derived using the formula for divergence and gradient in ellipsoidal coordinates as shown in Eqs. (28a) and (28b).

$$\nabla\theta = \frac{1}{c}\sqrt{\frac{\left(\xi^2 + 1\right)}{\left(\xi^2 + \eta^2\right)}}\frac{\partial \theta}{\partial \xi}\vec{i}_\xi, \quad \frac{\partial \theta}{\partial \eta} = 0 \tag{32a}$$

$$\nabla^2\theta = \frac{1}{c^2\left(\xi^2 + \eta^2\right)}\frac{\partial}{\partial \xi}\left[\left(\xi^2 + 1\right)\frac{\partial \theta}{\partial \xi}\right] \tag{32b}$$

$$\nabla \cdot (\theta\nabla\phi) = \frac{1}{c^2\left(\xi^2 + \eta^2\right)}\frac{\partial}{\partial \xi}\left[\left(\xi^2 + 1\right)\frac{\partial \phi}{\partial \xi}\theta\right] \tag{32c}$$

Using equation (32), the energy conservation Eq. (23b) can be expressed as shown below.

$$\frac{\partial \theta}{\partial t} + \frac{1}{c^2\left(\xi^2 + \eta^2\right)}\left\{\frac{\partial}{\partial \xi}\left[\left(\xi^2 + 1\right)\frac{d\phi}{d\xi}\theta\right] - \mathcal{D}\frac{\partial}{\partial \xi}\left[\left(\xi^2 + 1\right)\frac{\partial \theta}{\partial \xi}\right]\right\} = 0 \tag{33}$$

Eq. (31) can be substituted in (33), to get

$$\frac{\partial \theta}{\partial t} + \frac{1}{c^2\left(\xi^2 + \eta^2\right)}\frac{\partial}{\partial \xi}\left[\frac{\dot{M}}{4\pi c\rho}\theta - \mathcal{D}\left(\xi^2 + 1\right)\frac{\partial \theta}{\partial \xi}\right] = 0 \tag{34}$$

The equation becomes more concise when the non-dimensional Peclet number and time are introduced.

$$\mathrm{Pe}_c = \frac{\dot{M}}{(4\pi c)\rho\mathcal{D}}, \quad \tau = \frac{\mathcal{D}t}{c^2} \tag{35}$$

Then, the energy conservation equation can be expressed in terms of dimensionless parameters as follows:

$$\frac{\partial \theta}{\partial \tau} + \frac{1}{\left(\xi^2 + \eta^2\right)}\frac{\partial}{\partial \xi}\left[\mathrm{Pe}_c\theta - \left(\xi^2 + 1\right)\frac{\partial \theta}{\partial \xi}\right] = 0 \tag{36}$$

The boundary conditions for this problem are that the temperature is T_s on the surface of the ellipsoid given by $\xi = \xi_o$, and the temperature is T_∞ in the far field where $\xi \to \infty$, or

$$\theta(\xi = \xi_o, t) = 1, \ \theta(\xi \to \infty, t) = 0 \tag{37}$$

4.3. Composite solution

The composite transient solution for the ellipsoidal conduction problem is adopted from the solution presented for the spherical conduction problem with heated flow. This composite solution combines the steady state solution to the above problem near the ellipsoid with the far field transient solution.

The steady state equation follows from Eq. (37):

$$\frac{d}{d\xi}\left[\mathrm{Pe}_c\theta - \left(\xi^2+1\right)\frac{d\theta}{d\xi}\right] = 0 \tag{38}$$

Eq. (38) can be readily integrated to obtain,

$$\mathrm{Pe}_c\theta - \left(\xi^2+1\right)\frac{d\theta}{d\xi} = E \tag{39}$$

Here, E is a constant of integration. Eq. (39) is integrated by rearranging the terms and applying the boundary condition that $\theta = 0$ at $\xi \to \infty$. This gives,

$$\int_0^\theta \frac{d\theta}{\mathrm{Pe}_c\theta - E} = \int_\infty^\xi \frac{d\xi}{\xi^2+1} \tag{40}$$

The above integral can be simplified to the following form:

$$\frac{1}{\mathrm{Pe}_c}\ln\left[\frac{E}{E-\mathrm{Pe}_c\theta}\right] = \frac{\pi}{2} - \arctan(\xi) \tag{41}$$

The value of the constant E can be obtained by enforcing the boundary condition for the temperature on the ellipsoid surface, i.e., $\theta = 1$ at $\xi = \xi_o$.

$$E = \mathrm{Pe}_c\left\{1 - \exp\left[\mathrm{Pe}_c\left(\arctan(\xi_o) - \frac{\pi}{2}\right)\right]\right\}^{-1} \tag{42}$$

Thus, the final form of the steady state solution reduces to:

$$\theta = \frac{1 - \exp\left[\mathrm{Pe}_c\left(\arctan(\xi) - \frac{\pi}{2}\right)\right]}{1 - \exp\left[\mathrm{Pe}_c\left(\arctan(\xi_o) - \frac{\pi}{2}\right)\right]} \tag{43}$$

where $\mathrm{Pe}_c = \dot{M}/(4\pi c\rho\mathcal{D})$ is the Peclet number for the ellipsoidal conduction problem. Note that the steady state solution behaves as $1/\xi$.

The far field transient solution is developed from Eq. (36). The effect of the surface fluid flow is negligible because Pe is a much lower order compared to ξ. Also, since $\xi \to \infty$ in the far-field and $-1 \le \eta \le 1$, it is reasonable to assume that $\xi^2 + 1 \approx \xi^2$ and $\xi^2 + \eta^2 \approx \xi^2$. Hence, the transient energy Eq. (36) in the far field reduces to the form as shown below.

$$\frac{\partial\theta}{\partial\tau} = \frac{1}{\xi^2}\frac{\partial}{\partial\xi}\left(\xi^2\frac{\partial\theta}{\partial\xi}\right) \tag{44}$$

This form of partial differential equation has already been solved (Eq. (15)) and the analytical solution is given as:

$$\theta = \frac{1}{\xi}\mathrm{erfc}\left(\frac{\xi-\xi_o}{2\sqrt{\tau}}\right) \tag{45}$$

The above expression is the transient solution for the dimensionless temperature θ in the far-field. If the steady-state for Eq. (45) is considered, i.e., $\tau \to \infty$, θ varies with $1/\xi$. This shows that the error-function part of the solution is the transient component whereas the $1/\xi$ indicates the steady component. Hence, to get the composite solution in the entire domain, $1/\xi$ in Eq. (45) is replaced with the exact steady state solution derived in Eq. (43). The final solution for the dimensionless temperature can be written as,

$$\theta = \left\{\frac{1 - \exp\left[\mathrm{Pe}_c\left(\arctan(\xi) - \frac{\pi}{2}\right)\right]}{1 - \exp\left[\mathrm{Pe}_c\left(\arctan(\xi_o) - \frac{\pi}{2}\right)\right]}\right\}\mathrm{erfc}\left(\frac{\xi-\xi_o}{2\sqrt{\tau}}\right),$$

$$\mathrm{Pe}_c = \frac{\dot{M}}{(4\pi c)\rho\mathcal{D}} \tag{46}$$

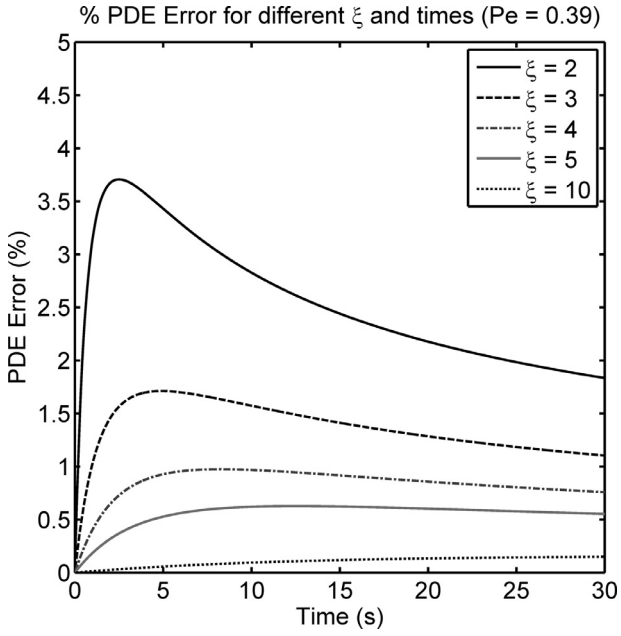

Fig. 9. PDE Error for the composite solution to the ellipsoidal conduction problem.

4.4. Error analysis

The composite transient solution to the ellipsoidal conduction problem with blowing is exact in the near field and the far field. The objective of the error analysis is to assess the accuracy of the solution in the entire domain. The accuracy of the transient ellipsoidal solution is tested by substituting the dimensionless temperature, as derived in Eq. (46), in the energy equation as given by Eq. (36). The error in the PDE, as previously defined in Section 3.3, is determined with time for different values of ξ. Since η does not appear in the final solution, an average value of $\eta^2 = 1/3$ is used.

The aspect ratio $\epsilon = 0$ is chosen here as the burner in the combustion problem will ultimately be approximated by a flat disk, A disk of diameter 25 mm is considered that has a fluid flowing through it at a surface mass flux of $\dot{m}''_o = 3.582\mathrm{g/m^2{-}s}$ corresponding to a Peclet number of 0.39, again representative of the combustion problem. The error in the energy equation is shown in Fig. 9. It can be seen that the error peaks at less than 4% for different values of ξ and at all times, rapidly decreasing as time increases. Thus, the accuracy of the approximate composite thermal solution has been tested here by the 'substitution' method, verified as sound by the full numerical solution in Section 3.

5. Ellipsoidal combustion model

The model used to study the combustion induced by the BRE burners in a microgravity environment can now be considered. The burner is replaced by a circular disk in an unbounded medium. A circular disk is the limiting form ($\epsilon = 0$) of an oblate ellipsoid of revolution. The introduction of oblate ellipsoidal coordinates together with the approximate composite solution approach developed in Sections 2–4 permits the construction of an analytical solution for the burner with a fixed flow rate of fuel in microgravity. Sections 2–4 justify the solution approach, and offer an explicit formula for parameters over the alternative numerical modeling. Of course, the real proof of the solution is how well it predicts the experimental data. The experimental data available is the transient behavior of the flame shape and the heat transfer to the surface of the burner for about 5 s in microgravity combustion.

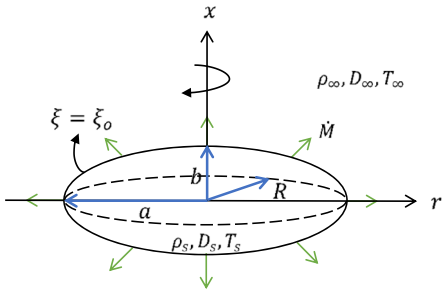

Fig. 10. Schematic and geometry of the ellipsoidal body.

The burning of fuel leaving the surface of an axially symmetric oblate ellipsoidal body is studied in a microgravity environment. The model considers fuel injected through the surface at a constant mass flow rate $\dot{M}$. The schematic and geometry of the ellipsoidal body is as shown in Fig. 10.

The ellipsoid surface is at a constant temperature T_s that is the vaporization temperature of the fuel. This temperature T_s corresponds to the density ρ_s and diffusivity $\mathcal{D}_s$. Initially at time $t = 0$, the environment surrounding the particle is at a constant temperature T_∞, density ρ_∞ and diffusivity $\mathcal{D}_\infty$. The flame that is initially at the surface starts spreading outwards while the density ρ, velocity u and temperature T vary in space and time.

5.1. Conservation laws

The temperature T and oxygen mass fraction Y_O are combined into a mixture fraction variable Z [39] which can be written as

$$Z = \frac{c_p(T - T_\infty) + \Delta h_c(Y_O - Y_{O,\infty})/S}{c_p(T_s - T_\infty) - \Delta h_c Y_{O,\infty}/S}, \tag{47}$$

or in alternate forms involving the species as will be shown later. Here, $Y_{O,\infty}$ is the ambient oxygen mass fraction, Δh_c is the heat of combustion per mass of fuel, c_p is the specific heat of the gas and S is the stoichiometric ratio which denotes the mass of oxygen consumed per unit mass of fuel. The mixture fraction model requires that the Lewis number $\mathrm{Le} \equiv k/\rho c_p \mathcal{D} = 1$. Then the energy and species conservation equations can be combined into a single mixture fraction equation. As in Section 4.2 the velocity is assumed to be represented by a potential function. The mass conservation and mixture fraction equations in ellipsoidal coordinates [40] now take the form with density variable (and following the Equation of State $\rho T = \rho_\infty T_\infty$):

$$\frac{\partial \rho}{\partial t} + \frac{1}{c^2\left(\xi^2 + \eta^2\right)} \frac{\partial}{\partial \xi}\left[\rho\left(\xi^2 + 1\right)\frac{\partial \phi}{\partial \xi}\right] = 0 \tag{48a}$$

$$\frac{\partial (\rho Z)}{\partial t} + \frac{1}{c^2\left(\xi^2 + \eta^2\right)}\left\{\frac{\partial}{\partial \xi}\left[\rho Z\left(\xi^2 + 1\right)\frac{\partial \phi}{\partial \xi}\right] - \frac{\partial}{\partial \xi}\left[\rho \mathcal{D}\left(\xi^2 + 1\right)\frac{\partial Z}{\partial \xi}\right]\right\} = 0 \tag{48b}$$

Here, ϕ is the velocity potential such that $\vec{u} = \nabla\phi$. The velocity potential ϕ is only a function of ξ as per the no-slip condition and the derivative of mixture fraction Z with respect to η is ignored as it is anticipated that the solution to be constructed is a function only of ξ and time so that $(\partial Z/\partial \eta = 0)$. The boundary conditions for this problem following its definition (47) are that the mixture fraction $Z = 1$ on the surface of the burner which is defined by $\xi = \xi_o$, and $Z = 0$ in the far field where $\xi \to \infty$. Also, the velocity potential ϕ takes a constant value along the burner due to no-slip condition, and in the far field takes the form,

$$\phi \sim -\frac{\dot{M}}{4\pi\rho|\vec{y}|} \tag{49a}$$

where $\dot{M}$ is the total mass flow rate leaving the particle surface and $|\vec{y}|$ is the distance from the burner center. For the BRE burner taken as the upper half of the ellipsoidal general surface, the velocity potential ϕ in the far field becomes,

$$\phi \sim -\frac{\dot{M}}{2\pi\rho|\vec{y}|}. \tag{49b}$$

5.2. Composite solution: steady

A composite solution is presented for the ellipsoidal combustion problem similar to the thermal solution Section 4. The steady state continuity and energy equations follow from Eqs. (48a) and (48b):

$$\frac{d}{d\xi}\left[\rho\left(\xi^2 + 1\right)\frac{d\phi}{d\xi}\right] = 0 \tag{50a}$$

$$\left\{\frac{d}{d\xi}\left[\rho Z\left(\xi^2 + 1\right)\frac{d\phi}{d\xi}\right] - \frac{d}{d\xi}\left[\rho\mathcal{D}\left(\xi^2 + 1\right)\frac{dZ}{d\xi}\right]\right\} = 0 \tag{50b}$$

Here ρ *and* $\rho\mathcal{D}$ are assumed to be functions of Z. Eqs. (50a) and (50b) can be readily integrated, similar to the derivation in Section 4.3, and the boundary conditions can be applied to get the final form of the steady state solution. Eq. (50a) is integrated with the constant of integration evaluated for the mass flow rate through the upper surface of the ellipsoid or burner disc in the limit:

$$\rho\left(\xi^2 + 1\right)\frac{d\phi}{d\xi} = \frac{\dot{M}}{2\pi c} \tag{51a}$$

Similarly, a first integral of Eq. (50b) can be found in the form:

$$\frac{\dot{M}}{2\pi c} Z(\xi) - \rho\mathcal{D}(\xi^2 + 1)\frac{dZ}{d\xi} = constant \tag{51b}$$

In this scenario, for the sake of simplicity, $\rho\mathcal{D}$ is taken as a constant, $\rho_\infty \mathcal{D}_\infty$, as that is a common assumption for gases. This is in effect a statement about the temperature dependence of the diffusivity. Then Eq. (51b) takes the form of Eq. (39), and operating as before in Eqs. (40)–(42), the steady solution follows for Z.

$$Z = \frac{1 - \exp\left[\mathrm{Pe}_c\left(\arctan(\xi) - \frac{\pi}{2}\right)\right]}{1 - \exp\left[\mathrm{Pe}_c\left(\arctan(\xi_o) - \frac{\pi}{2}\right)\right]} \tag{52}$$

Here, $\mathrm{Pe}_c = \frac{\dot{M}}{2\pi c \rho_\infty \mathcal{D}_\infty}$ is the effective Peclet number for the upper ellipsoidal combustion problem. Note that $\xi_o = \frac{\epsilon}{\sqrt{1-\epsilon^2}}$ *and* $c = R\sqrt{1-\epsilon^2}$.

5.3. Composite solution: transient

To get the far field transient solution, as in 4.3, the velocity is small $(\vec{u} \to 0)$ and the density now approaches a constant, ρ_∞. Also since $\xi \to \infty$ in the far-field and $-1 \le \eta \le 1$, it is reasonable to take $\xi^2 + 1 \approx \xi^2$ and $\xi^2 + \eta^2 \approx \xi^2$. Hence, the mixture fraction transient Eq. (48b) in the far field reduces to

$$\rho_\infty \frac{\partial Z}{\partial t} = \rho_\infty \mathcal{D}_\infty \frac{1}{c^2\xi^2}\frac{\partial}{\partial \xi}\left(\xi^2 \frac{\partial Z}{\partial \xi}\right) \tag{53}$$

This partial differential equation has a solution as shown in Sections 3.1 and 4.3, and it is given as:

$$Z = \frac{1}{\xi}\mathrm{erfc}\left(\frac{\xi - \xi_o}{2\sqrt{\tau}}\right), \quad \tau = \frac{\mathcal{D}_\infty t}{c^2} \tag{54}$$

The above expression is the transient solution for the ellipsoidal combustion problem in the far-field. If the steady-state for Eq. (54) is considered, i.e., $\tau \to \infty$, Z varies with $1/\xi$. This shows that the error function part of the solution is the transient component whereas the $1/\xi$ indicates the steady component. Hence, to get the composite solution in the entire domain, $1/\xi$ in Eq. (54) is replaced with the exact steady state solution derived in Eq. (52). Hence, the final solution for the mixture fraction can be written as,

$$Z = \left\{ \frac{1 - \exp\left[\mathrm{Pe}_c\left(\arctan(\xi) - \frac{\pi}{2}\right)\right]}{1 - \exp\left[\mathrm{Pe}_c\left(\arctan(\xi_o) - \frac{\pi}{2}\right)\right]} \right\} \mathrm{erfc}\left(\frac{\xi - \xi_o}{2\sqrt{\tau}}\right),$$

$$\mathrm{Pe}_c = \frac{\dot{M}}{2\pi c \rho_\infty \mathcal{D}_\infty} \tag{55}$$

5.4. Variation of temperature and species mass fractions

A piecewise linear state relation given by Eq. (55) expresses the mixture fraction in terms of the temperature and oxygen mass fraction. Further state relations are chosen to connect the fuel mass fraction and products mass fraction to the mixture fraction as shown below.

$$Z = \frac{SY_F - (Y_O - Y_{O,\infty})}{SY_{Fb} + Y_{O,\infty}} \tag{56a}$$

$$Z = \frac{(1+S)Y_F + Y_P}{(1+S)Y_{Fb} + Y_{Pb}} \tag{56b}$$

The quantities Y_{Fb} and Y_{Pb} denote the fuel and product mass fractions at the burner surface respectively. The state relations emerge from the assumptions of Fick's Law of diffusion and equal diffusivity for all species, a plausible approximation if nitrogen is the dominant molecular species as in the experiments. These relations satisfy the mixture fraction equation and the boundary conditions.

The combustion reaction assumed to be infinitely fast such that the oxidizer and fuel cannot coexist. This is the classical thin flame assumption to circumvent the need for explicit chemical kinetics. The fuel and oxygen are separated by the infinitesimally thin flame sheet that is located by,

$$Z = Z_{fl} = \frac{Y_{O,\infty}}{SY_{Fb} + Y_{O,\infty}} \tag{57}$$

The above value of the mixture fraction at the flame sheet can be substituted in the composite solution given by Eq. (55) to obtain the flame position ξ_{fl}.

Since the thin flame sheet separates the fuel and the oxygen, the reaction zone can be divided into two domains, i.e., the oxidizer side and the fuel side. On the fuel side of the flame where $\xi_o \le \xi \le \xi_{fl}$ and $Z \ge Z_{fl}$, the species mass fractions can be expressed as:

$$Y_O = 0,$$
$$Y_F = ZY_{Fb} - (1-Z)Y_{O,\infty}/S,$$
$$Y_P = ZY_{Pb} + (1-Z)(1+S)Y_{O,\infty}/S,$$
$$T = T_\infty + Z(T_s - T_\infty) + (1-Z)\left(\frac{\Delta h_c Y_{O,\infty}}{Sc_p}\right). \tag{58}$$

Similarly, on the oxidizer side of the flame where $\xi_{fl} \le \xi < \infty$ and $Z \le Z_{fl}$, the species mass fractions are given as shown below.

$$Y_F = 0,$$
$$Y_O = (1-Z)Y_{O,\infty} - SZY_{Fb},$$
$$Y_P = Z[(1+S)Y_{Fb} + Y_{Pb}],$$
$$T = T_\infty + Z(T_s - T_\infty) + Z\left(\frac{\Delta h_c Y_{Fb}}{c_p}\right). \tag{59}$$

In the expressions for the temperature and the species mass fractions, $Y_{O,\infty}$ is the ambient oxygen mass fraction which is known whereas the fuel and product mass fractions at the surface, Y_{Fb} and Y_{Pb}, respectively, are not known. In order to determine Y_{Fb}, it is required that the fuel mass flux crossing the ellipse surface at steady-state is equal to that carried away by advection and diffusion. This can be expressed as:

$$Y_{Fb}\left(\rho\frac{\partial\phi}{\partial\xi}\right)_{\xi=\xi_o} - \rho\mathcal{D}\left(\frac{\partial Y_F}{\partial\xi}\right)_{\xi=\xi_o} = \left(\rho\frac{\partial\phi}{\partial\xi}\right)_{\xi=\xi_o} \tag{60}$$

In the above equation, $\rho\mathcal{D}$ is a constant and the *steady* mass flux of fuel supplied through the upper surface is given by Eq. (51) as,

$$\dot{m}'' = \left(\rho\frac{\partial\phi}{\partial\xi}\right)_{\xi=\xi_o} = \frac{\dot{M}}{2\pi c\left(\xi_o{}^2 + 1\right)} = \rho\mathcal{D}\frac{\mathrm{Pe}_c}{\xi_o{}^2 + 1} \tag{61}$$

Hence, to determine Y_{Fb}, it is necessary to compute the value of $(\partial Y_F/\partial\xi)_{\xi=\xi_o}$ at steady-state. The steady-state solution for the mixture fraction Z given by Eq. (52) can be differentiated and its value at the surface of the particle is given as:

$$\left(\frac{dZ}{d\xi}\right)_{\xi=\xi_o,\ t\to\infty} = -\left(\frac{\mathrm{Pe}_c}{\xi_o{}^2 + 1}\right)\left\{\frac{\exp\left[\mathrm{Pe}_c\left(\arctan(\xi_o) - \frac{\pi}{2}\right)\right]}{1 - \exp\left[\mathrm{Pe}_c\left(\arctan(\xi_o) - \frac{\pi}{2}\right)\right]}\right\} \tag{62}$$

The expression for the fuel mass fraction given in Eq. (58) can be differentiated to obtain the following relation.

$$\left(\frac{\partial Y_F}{\partial\xi}\right)_{\xi=\xi_o} = \left(\frac{SY_{Fb} + Y_{O,\infty}}{S}\right)\left(\frac{\partial Z}{\partial\xi}\right)_{\xi=\xi_o} \tag{63}$$

Thus, combining Eqs. (62) and (63) provides the value for $(\partial Y_F/\partial\xi)_{\xi=\xi_o}$ which is substituted in Eq. (60) along with Eq. (61) to obtain the fuel mass fraction at the surface Y_{Fb}.

$$Y_{Fb} = 1 - \left(\frac{Y_{O,\infty} + S}{S}\right)\exp\left[\mathrm{Pe}_c\left(\arctan(\xi_o) - \frac{\pi}{2}\right)\right] \tag{64}$$

The product mass fraction at the surface Y_{Pb} requires that the advection and diffusion of combustion products at the surface counterbalance each other. Thus, in the same way as the derivation of the fuel mass fraction, the product mass fraction at the surface Y_{Pb} can be obtained.

$$Y_{Pb} = Y_{O,\infty}\left(\frac{1+S}{S}\right)\exp\left[\mathrm{Pe}_c\left(\arctan(\xi_o) - \frac{\pi}{2}\right)\right] \tag{65}$$

These values for Y_{Fb} and Y_{Pb} complete the solution for temperature and mass fractions.

5.5. Surface heat flux distribution

The heat flux to the surface of the burner is measured during the microgravity experiments. The analytical transient behavior of the heat flux at the surface of the ellipsoidal burner can be derived. The starting point is the coordinate independent representation of the surface heat flux.

$$\dot{q}_s'' = -k|\nabla T|_s \tag{66}$$

Here, k is the thermal conductivity of the fluid and s represents the burner surface. To simplify Eq. (66) in oblate ellipsoidal coordinates, it is necessary to express the gradient of temperature $T(\xi)$.

$$\nabla T(\xi) = \frac{1}{c}\sqrt{\frac{(\xi^2+1)}{(\xi^2+\eta^2)}}\frac{\partial T}{\partial\xi}\vec{i}_\xi \tag{67}$$

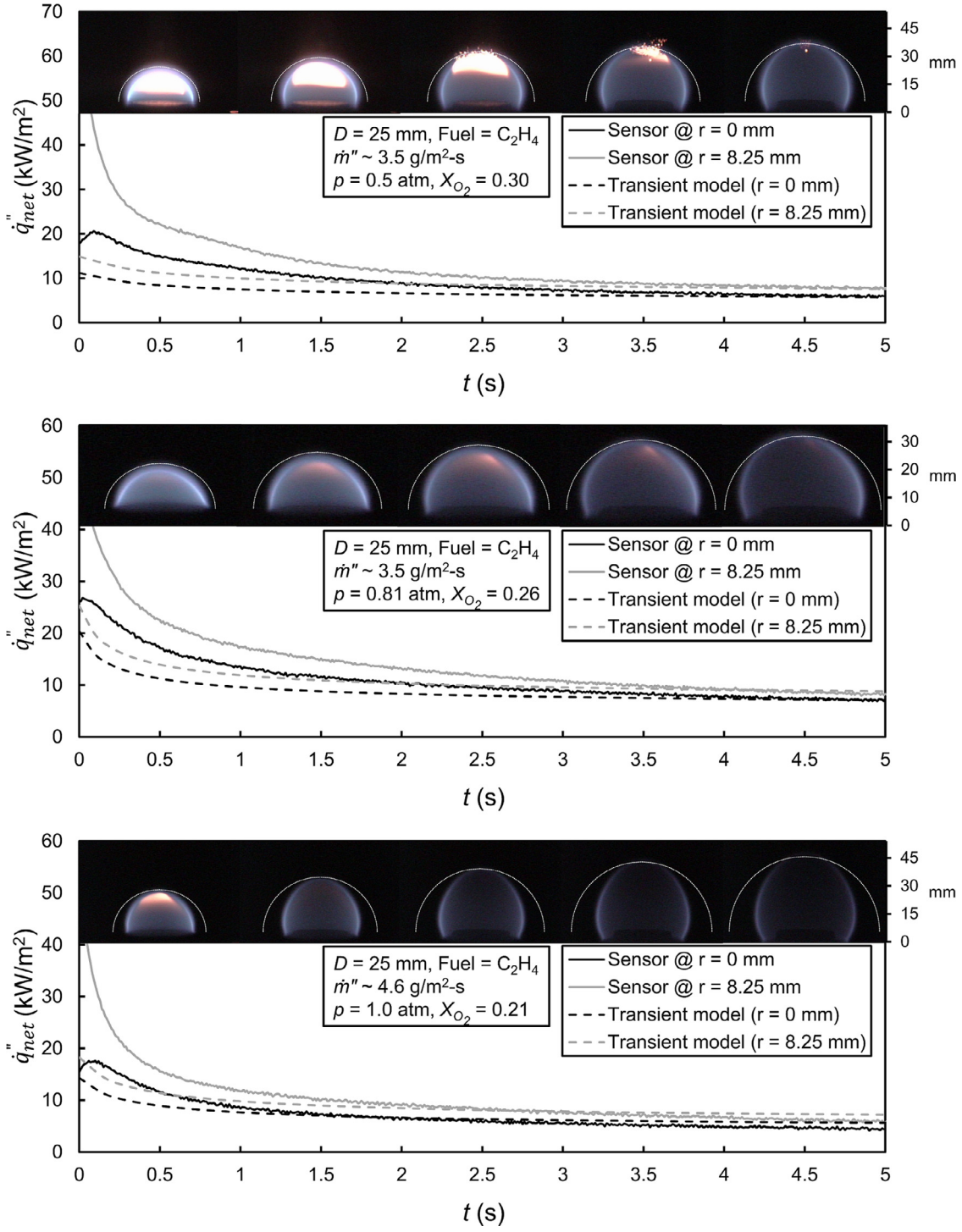

Fig. 11. Comparison of 5-s microgravity tests with the transient model for the 25 mm burner.

$\vec{i}_\xi$ denotes the unit vector normal to the surface of ellipsoid defined by ξ. The temperature gradient can be related to the differential of mixture fraction from Eq. (47).

$$\frac{\partial T}{\partial \xi} = \left[(T_s - T_\infty) - \frac{\Delta h_c Y_{O,\infty}}{S c_p} \right] \left(\frac{\partial Z}{\partial \xi} \right) \tag{68}$$

The gradient of temperature $T(\xi)$ can then be expressed as:

$$\nabla T(\xi) = \frac{1}{c} \sqrt{\frac{(\xi^2+1)}{(\xi^2+\eta^2)}} \left[(T_s - T_\infty) - \frac{\Delta h_c Y_{O,\infty}}{S c_p} \right] \frac{\partial Z}{\partial \xi} \vec{i}_\xi \tag{69}$$

Since surface heat flux is the desired quantity, the temperature gradient at the burner surface, defined by $\xi = \xi_o$, can be written as:

$$\nabla T(\xi = \xi_o) = \frac{1}{c} \sqrt{\frac{(\xi_o{}^2+1)}{(\xi_o{}^2+\eta^2)}} \left[(T_s - T_\infty) - \frac{\Delta h_c Y_{O,\infty}}{S c_p} \right] \left(\frac{\partial Z}{\partial \xi} \right)_{\xi=\xi_o} \vec{i}_{\xi_o} \tag{70}$$

The transient composite solution for the mixture fraction given by Eq. (55) can be differentiated and its value at the surface of the

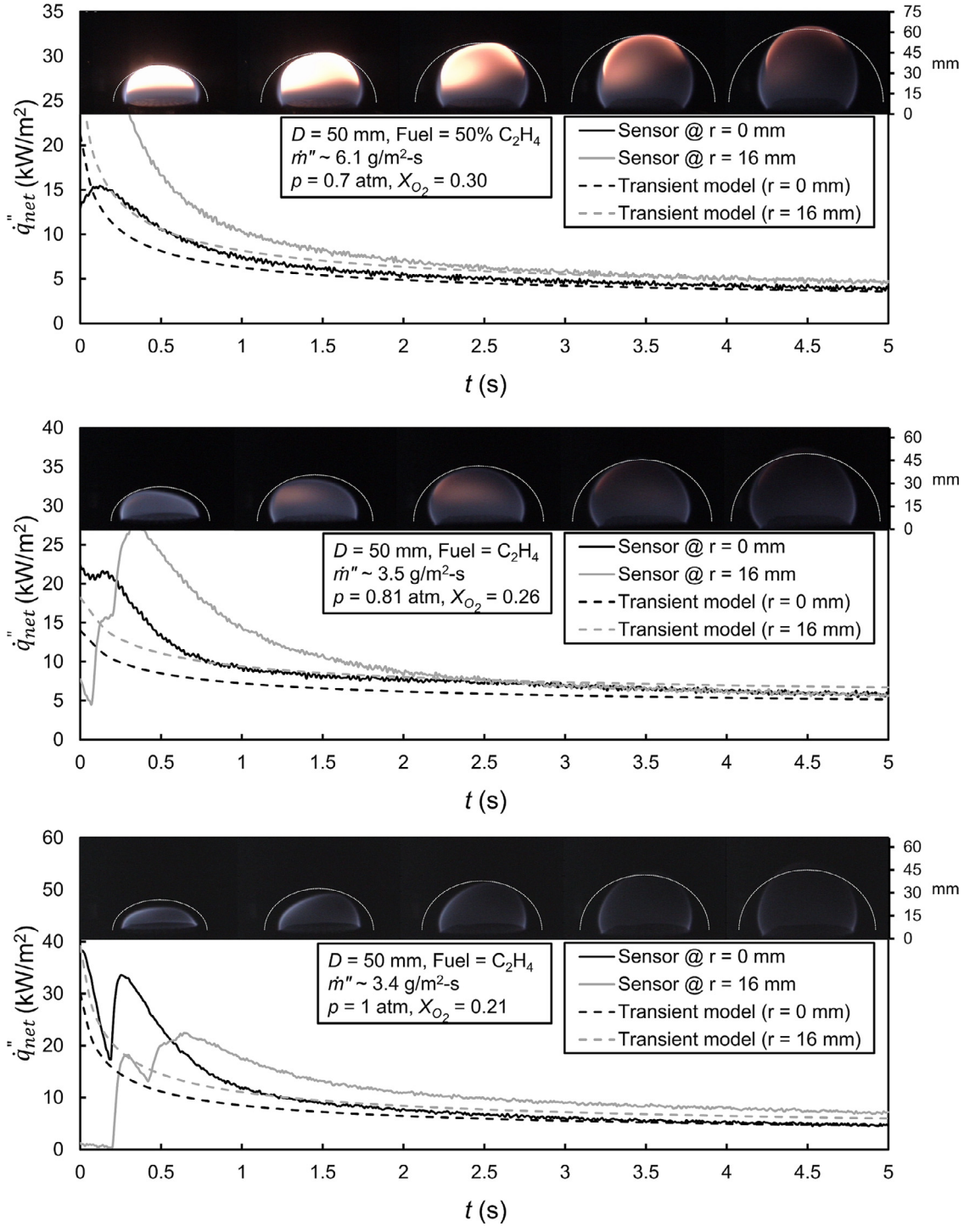

Fig. 12. Comparison of 5-s microgravity tests with the transient model for the 50 mm burner.

ellipsoid body is given as:

$$\left(\frac{\partial Z}{\partial \xi}\right)_{\xi=\xi_o} = -\frac{1}{\sqrt{\pi\tau}} - \left(\frac{\mathrm{Pe}_c}{{\xi_o}^2+1}\right)\left\{\frac{\exp\left[\mathrm{Pe}_c\left(\arctan\left(\xi_o\right)-\frac{\pi}{2}\right)\right]}{1-\exp\left[\mathrm{Pe}_c\left(\arctan\left(\xi_o\right)-\frac{\pi}{2}\right)\right]}\right\} \tag{71}$$

The radial heat flux distribution is considered by introducing the cylindrical variable r to replace the ellipsoidal variable η.

$$\eta^2 = 1 - \left(\frac{r}{R}\right)^2 \tag{72}$$

Also, the aspect ratio of the ellipsoid body ϵ can be related to the surface ellipse ξ_o and the variable c using the following equations.

$$\xi_o = \frac{\epsilon}{\sqrt{1-\epsilon^2}}, \quad c = R\sqrt{1-\epsilon^2} \tag{73}$$

Thus, the analytical transient heat flux distribution at the surface of the ellipsoid body (defined by $\xi = \xi_o$) takes the final form:

$$\dot{q}_s''(r) = \frac{\dot{q}_s''(r=0)}{\sqrt{1-\left(1-\epsilon^2\right)(r/R)^2}}, \tag{74}$$

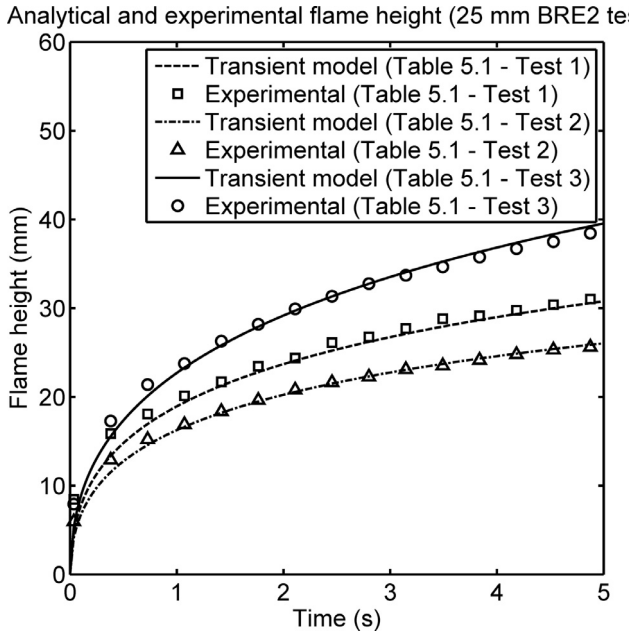

Fig. 13. Comparison of analytical and experimental flame height for the 25 mm burner microgravity tests.

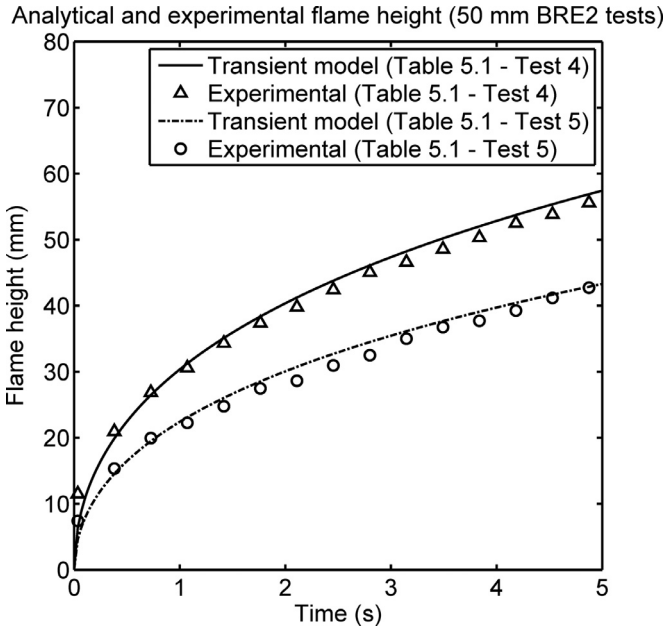

Fig. 14. Comparison of analytical and experimental flame height for the 50 mm burner microgravity tests.

where

$$\dot{q}_s''(r=0) = -\frac{k}{R\sqrt{1-\epsilon^2}}\left[(T_s - T_\infty) - \frac{\Delta h_c Y_{O,\infty}}{Sc_p}\right]A_\epsilon,$$

$$A_\epsilon = \frac{1}{\sqrt{\pi\tau}} + \mathrm{Pe}_c\left(1-\epsilon^2\right)\left\{\frac{\exp\left[\mathrm{Pe}_c\left(\arctan\left(\frac{\epsilon}{\sqrt{1-\epsilon^2}}\right)-\frac{\pi}{2}\right)\right]}{1-\exp\left[\mathrm{Pe}_c\left(\arctan\left(\frac{\epsilon}{\sqrt{1-\epsilon^2}}\right)-\frac{\pi}{2}\right)\right]}\right\}.$$

The BRE burner surface under study is a flat disk. The geometry of a disk is the limiting configuration of the oblate ellipsoid. The heat flux distribution at the surface of the burner with ellipsoidal aspect ratio $\epsilon = 0$ can be expressed as follows:

$$\dot{q}_s''(r) = \frac{\dot{q}_s''(r=0)}{\sqrt{1-(r/R)^2}} \tag{75}$$

where

$$\dot{q}_s''(r=0) = -\frac{k}{R}\left[(T_s - T_\infty) - \frac{\Delta h_c Y_{O,\infty}}{Sc_p}\right]A_{\epsilon=0},$$

$$A_{\epsilon=0} = \frac{1}{\sqrt{\pi\tau}} + \mathrm{Pe}_c\left[\frac{\exp\left(-\frac{\pi}{2}\mathrm{Pe}_c\right)}{1-\exp\left(-\frac{\pi}{2}\mathrm{Pe}_c\right)}\right].$$

The direction of the heat flux is normal to the flat burner disk. It is interesting to note that the surface heat flux follows an inverse square-root distribution with the least value at the center of the disk. This dependence has been shown to accurately represent the data by Markan et al. [4].

6. Prediction of 5-s microgravity tests

The BRE burner, as described in the Introduction and literature [1-4], was tested at NASA Glenn's 5.18-s Zero Gravity Research Facility and flame growth along with surface heat flux were recorded. The flames were found to be nearly hemispherical within 5 s, with the flame height still increasing. The heat flux initially fell quickly and then became steadier. The results of the BRE microgravity experiments are utilized to investigate the accuracy of the transient mathematical model. During these experiments, fuel at a constant mass flux is passed through the burner surface. This is the condition of the transient model. The burner geometry can be idealized as an axially symmetric flat porous disk with fuel flowing out from one side so as to apply the ellipsoidal model. Several representative

Table 1
Microgravity tests to study the ellipsoidal combustion model.

Test no.	D (mm)	Fuel	X_{O_2}	p (atm)	$\dot{m}''$ (g/m^2-s)	T_s (°C)
1	25	C_2H_4	0.30	0.5	3.53	34.5
2	25	C_2H_4	0.26	0.81	3.46	32.9
3	25	C_2H_4	0.21	1.0	4.65	32.7
4	50	50% C_2H_4	0.3	0.7	6.14	80.7
5	50	C_2H_4	0.26	0.81	3.47	89.0
6	50	C_2H_4	0.21	1.0	3.41	135.3

25 mm and 50 mm diameter burner tests are selected for comparison with the model. The parameters for these tests are shown in Table 1 and form the input to the mathematical model. The product of density and diffusivity ($\rho\mathcal{D}$) is taken as a constant and its value is fixed at 6×10^{-5} kg/m-s. Also, the value of thermal conductivity (k) is fixed at 0.07 W/m-K, specific heat at 1.167 kJ/kg-K and Δh_c, S depend on the fuel used during the test. Since the BRE burner is idealized as a flat disk, the ellipsoidal aspect ratio ϵ is taken as 0. The measurements during the test include the heat flux and the temperature at two locations on the burner surface, one at the center and the other at an offset radius R^* ($R^* = 8.25$ mm for the 25 mm burner, $R^* = 16$ mm for the 50 mm burner). The flame shape is recorded using analog video. The surface temperature during the 5 s test does not change by much and hence, it can be taken as a constant input for the mathematical model.

It is important to account for the fact that the experiment runs for only about 5 s and a steady flame is not achieved during the test. Hence, the transient model would provide a prediction of the flame shape and heat flux beyond the duration of the test. The composite transient solution presented in Section 5.2 is utilized to provide a prediction of the flame shape and the heat flux for the 5 s drop tests. The ellipsoidal flame location ξ_{fl} is obtained by substituting the mixture fraction value Z_{fl} at the flame in the composite solution. The heat flux at the surface is obtained using the formula derived in Section 5.4. Figures 11 and 12 show the predicted heat flux and flame shape for the tests listed in Table 1. The predicted flame shape is denoted by dotted lines superimposed over the flame images. The flame images are taken at each 1-second interval. The graph shows the predicted heat flux at the surface

along with the experimental heat flux at the two locations. There is good agreement between the predicted heat flux and the experimental heat flux after the initial two seconds. The initial differences are due to the transformation of the initial 1 g flame to a microgravity flame during the 5 s experiment. So the experiment does not have the initial condition of the model. The flame height y_f, i.e., the location of the flame above the center of the burner, is derived from the ellipsoidal flame location ξ_{fl} and compared with the experimental values. This is done for the 25 mm BRE2 tests in Fig. 13 and the 50 mm BRE2 tests in Fig. 14. Test 6 from Table 1 is not plotted in Fig. 14 since it closely resembles the flame growth of Test 5. It can be seen for 25 mm and 50 mm tests that the ellipsoidal combustion model closely predicts the flame height. The 5-s flame height reaches about 30 – 40% of the predicted steady-state height.

The ISS tests are designed to examine if a steady state can be achieved. Radiation loss from the flame and extinction are not included in the current model so it is not clear how this can be extrapolated to longer time durations. But the model accurately predicts the flame shape and heat flux for the microgravity BRE experiments up to 5-s.

7. Conclusions

A transient approximate mathematical model for the BRE microgravity flame is presented. It is based on an axisymmetric model that predicts the quasi-steady burning of small firebrands that employs oblate ellipsoidal coordinates. This coordinate system greatly simplifies the problem to one space dimension. The approximate analytical transient solution is generated by multiplying an exact steady-state solution with a far-field asymptotic transient solution. The combustion model is justified by analyses of constant property heat transfer problems where comparison with a numerical solution is very good and theoretical substitution error is very small. The combustion model accurately predicts the flame shape and heat flux for the microgravity BRE experiments up to the 5-second ground test durations. The model also correctly demonstrated that the surface heat flux approaches steady state faster than the flame length, and may be near steady state at the 5 s experimental end point. Hence, the assumption of steady state for the heat flux at 5 s to derive an effective heat of gasification for steady burning may be reasonable. However, longer ISS experiments will be telling.

The five second ground duration was not sufficient to detect any radiative extinguishment or cool flames. However, radiation might become dominant in the ISS flames due to their extended burn time and bigger flame shapes. Barring radiative extinguishment, the ISS flames burning for 60 s are estimated to reach about 90% of their steady-state positions. Future work will include the effects of radiation in the unsteady combustion model as a basis for analysis of the ISS tests.

Declaration of Competing Interest

There are no declarations of interest for the authors listed in this manuscript.

Acknowledgments

This research was funded by NASA's International Space Station Research Program (grant number NNX15AD06A), with D.P. Stocker serving as contract monitor.

References

[1] Y. Zhang, M. Kim, P.B. Sunderland, J.G. Quintiere, J.L. de Ris, A burner to emulate condensed phase fuels, Exp. Therm. Fluid Sci. 73 (5) (2016) 87–93.
[2] Y. Zhang, M. Kim, H. Guo, P.B. Sunderland, J.G. Quintiere, J.L. de Ris, D.P. Stocker, Emulation of condensed fuel flames with gases in microgravity, Combust. Flame 162 (10) (2015) 3449–3455.
[3] A. Markan, P.B. Sunderland, J.G. Quintiere, J.L. de Ris, D.P. Stocker, H.R Baum, A Burning Rate Emulator (BRE) for study of condensed fuel burning in microgravity, Combust. Flame 192 (2018) 272–282.
[4] A. Markan, P.B. Sunderland, J.G. Quintiere, J.L. de Ris, H.R. Baum, Measuring heat flux to a porous burner in microgravity, Proc. Combust. Inst. (2018), doi:10.1016/j.proci.2018.05.006.
[5] A.M. Kanury, Introduction to combustion phenomena, Gordon and Breach, Amsterdam, 1975.
[6] M. Klajn, A.K. Oppenheim, Influence of exothermicity on the shape of a diffusion flame, Symp. (Int.) Combust. 19 (1982) 223–235.
[7] S.H. Chung, C.K. Law, Burke-Schumann flame with streamwise and preferential diffusion, Combust. Sci. Technol. 37 (1) (1984) 21–46.
[8] K.K. Kuo, Principles of combustion, Wiley, New York, 1986.
[9] S. Mahalingam, J.H. Ferziger, B.J. Cantwell, Self-similar diffusion flame, Combust. Flame 82 (2) (1990) 231–234.
[10] E. Villermaux, D. Durox, On the physics of jet diffusion flames, Combust. Sci. Technol. 84 (1) (1992) 279–294.
[11] D.L. Urban, Z.-G. Yuan, P.B. Sunderland, G.T. Linteris, J.E. Voss, G.M. Faeth, Structure and soot properties of nonbuoyant ethylene/air laminar jet diffusion flames, AIAA J. 36 (8) (1998) 1346–1360.
[12] K.-C. Lin, G.M. Faeth, P.B. Sunderland, D.L. Urban, Z.-G. Yuan, Shapes of nonbuoyant round luminous hydrocarbon/air laminar jet diffusion flames, Combust. Flame 116 (1999) 415–431.
[13] P.B. Sunderland, B.J. Mendelson, Z.-G. Yuan, D.L. Urban, Shapes of buoyant and nonbuoyant laminar jet diffusion flames, Combust. Flame 116 (1999) 376–386.
[14] F. Xu, Z. Dai, G.M. Faeth, Flame and soot boundaries of laminar jet diffusion flames, AIAA J. 40 (12) (2002) 2439–2446.
[15] C. Aalburg, F.J. Diez, G.M. Faeth, P.B. Sunderland, D.L. Urban, Z.-G. Yuan, Shapes of nonbuoyant round hydrocarbon-fueled laminar-jet diffusion flames in still air, Combust. Flame 142 (2005) 1–16.
[16] M.D. Smooke, R.J. Hall, M.B. Colket, J. Fielding, M.B. Long, C.S. McEnally, L.D. Pfefferle, Investigation of the transition from lightly sooting towards heavily sooting co-flow ethylene diffusion flames, Combust. Theor. Model. 8 (3) (2004) 593–606.
[17] X. Qin, C.W. Choi, A. Mukhopadhyay, I.K. Puri, S.K. Aggarwal, V.R. Katta, Triple flame propagation and stabilization in a laminar axisymmetric jet, Combust. Theor. Model. 8 (2) (2004) 1364–7830.
[18] S.S. Krishnan, J.M. Abshire, P.B. Sunderland, Z.-G. Yuan, J.P. Gore, Analytical predictions of shapes of laminar diffusion flames in microgravity and earth gravity, Combust. Theor. Model. 12 (4) (2008) 605–620.
[19] S.P. Burke, T.E.W. Schumann, Diffusion flames, Ind. Eng. Chem. 29 (1928) 998.
[20] F.G. Roper, The prediction of laminar jet diffusion flame sizes: part I. Theoretical model, Combust. Flame 29 (1977) 219–226.
[21] F.G. Roper, C. Smith, A.C. Cunningham, The prediction of laminar jet diffusion flame sizes: part II. Experimental verification, Combust. Flame 29 (1977) 227–234.
[22] D.B. Spalding, Combustion and mass transfer, Pergamon Press, 1979.
[23] A. Markan, Development and analysis of a Burning Rate Emulator (BRE) for study in microgravity Ph.D. thesis, , University of Maryland, College Park, 2018.
[24] K. Mills, M. Matalon, Burner-generated spherical diffusion flames, Combust. Sci. Technol. 129 (1) (1997) 295–319.
[25] K. Mills, M. Matalon, Extinction of spherical diffusion flames in the presence of radiant loss, Symp. (Int.) Combust. 27 (1998) 2535–2541.
[26] A. Atreya, S. Agrawal, K.R. Sacksteder, H.R. Baum, Observations of methane and ethylene diffusion flames stabilized around a blowing porous sphere under microgravity conditions, AIAA, 32nd Aerospace Sciences Meeting and Exhibit, Reno, 1994, pp. 1–10.
[27] A. Atreya, S. Agrawal, T. Shamim, K. Pickett, K.R. Sacksteder, H.R. Baum, Radiant extinction of gaseous diffusion flames, Proceedings of the 3rd International Microgravity Combustion Workshop, NASA Glenn Research Center, Cleveland, 1995, pp. 319–325.
[28] A. Atreya, S. Agrawal, Effect of radiative heat loss on diffusion flames in quiescent microgravity atmosphere, Combust. Flame 115 (3) (1998) 372–382.
[29] A. Atreya, S. Berhan, M. Chernovsky, K.R. Sacksteder, Unsteady spherical diffusion flames in microgravity, Proceedings of the 6th International Microgravity Combustion Workshop, NASA Glenn Research Center, Cleveland, 2001, pp. 113–116.
[30] M.K. Chernovsky, A. Atreya, H.G. Im, Effect of CO2 diluent on fuel versus oxidizer side of spherical diffusion flames in microgravity, Proc. Combust. Inst. 31 (1) (2007) 1005–1013.
[31] S.D. Tse, D. Zhu, C.J. Sung, Y. Ju, C.K. Law, Microgravity burner-generated spherical diffusion flames: experiment and computation, Combust. Flame 125 (4) (2001) 1265–1278.
[32] K.J. Santa, B.H. Chao, P.B. Sunderland, D.L. Urban, D.P. Stocker, R.L. Axelbaum, Radiative extinction of gaseous spherical diffusion flames in microgravity, Combust. Flame 151 (4) (2007) 665–675.
[33] K.J. Santa, Z. Sun, B.H. Chao, P.B. Sunderland, R.L. Axelbaum, D.L. Urban, D.P. Stocker, Numerical and experimental observations of spherical diffusion flames, Combust. Theor. Model. 11 (4) (2007) 639–652.
[34] R.J. Kee, J.F. Grcar, M.D. Smooke, J.A. Miller, A Fortran program for modeling steady laminar one-dimensional premixed flames, Sandia National Laboratories, 1985 Sandia Report SAND 85-8240.

[35] A.J. Bhowal, B.K. Mandal, Numerical simulation of transient development of flame, temperature and velocity under reduced gravity in a methane air diffusion flame, Microgravity Sci. Technol. 29 (1) (2017) 151–175.
[36] M.D. Smooke, R.E. Mitchell, D.E. Keyes, Numerical solution of two-dimensional axisymmetric laminar diffusion flames, Combust. Sci. Technol. 67 (1989) 85–122.
[37] M.D. Smooke, V. Giovangigli, Numerical modeling of axisymmetric laminar diffusion flames, Impact Comput. Sci. Eng. 4 (1) (1992) 46–79.
[38] R.V. Fursenko, S.S. Minaev, K.C. Chang, Y.C. Chao, Analytical and numerical modeling of a spherical diffusion microflame, Combust. Expl. Shock Waves 44 (1) (2008) 1–8.
[39] H. Baum, A. Atreya, A Model for Combustion of Firebrands of Various Shapes, Fire Saf. Sci. 11 (2014) 1353–1367.
[40] W. Magnus, F. Oberhettinger, Formulas and theorems for the functions of mathematical physics, Chelsea, New York, 1943, p. 149.
[41] S. Goldstein, Lectures on fluid mechanics, Interscience, New York, 1960, p. 89.
[42] H.S. Carslaw, J.C. Jaeger, Conduction of heat in solids, 2nd ed., Oxford University Press, London, 1959, p. 215.